Compact spatially heterodyned static interferometer

E. A. McCormack, A. Hugh Mortimer and L. Ciaffoni

Published version information

Citation: EA McCormack, AH Mortimer and L Ciaffoni. "Compact spatially heterodyned static interferometer." Applied Optics, vol. 59, no. 14 (2020): 4271.

DOI: 10.1364/AO.389949

Compact spatially-heterodyned static interferometer

E. A. McCormack, [1,*] A. Hugh Mortimer, [1] and L. Ciaffoni [1]

[1] *RAL Space, STFC Rutherford Appleton Laboratory, Harwell Oxford Campus, Didcot, OX11 0QX, United Kingdom*
[*] *elin.mccormack@stfc.ac.uk*

Abstract: This paper presents a novel and simple technique for achieving a higher spectral resolution in classical static Fourier transform spectrometers. This is achieved by heterodyning the frequency of a standard interferogram to a lower spatial frequency by placing a single transmission grating at the image plane of two mutually coherent beams produced by the interferometer. The grating splits the beams into diffraction orders which overlap to produce the heterodyned interferogram, similar to that seen in techniques such as Spatial Heterodyne Spectroscopy. The increase in spectral resolution for such a system is shown to be related to the angle between the beams and the groove period of the transmission grating. The theoretical performance of this design is compared to a proof of concept system that has been built using off-the-shelf components and tested at visible wavelengths. The experimental results agree well with those produced from a theoretical simulation.

1. Introduction

It is well established that the Fourier transform spectrometer (FTS) has many fundamental advantages over the diffractive spectrometer, such as higher throughput and resolving power [1]. A general trade-off between the most common type of FTS instrument, the Michelson FTS, and common diffractive spectrometers is that the high resolution of the Michelson FTS is reliant on moving optical components to generate the optical path difference (OPD) needed to record the interferogram at a single detector. One type of FTS that overcomes the need of moving optics is that of a static interferometer design. The static FTS has all optical components in fixed positions and arranged so that an entire interferogram is projected in space so that it can be recorded by an array detector without the need to introduce a variable optical path difference by scanning one of the mirrors. The static interferometer has two main advantages: (i) it can be rugged, compact and lightweight; (ii) it may achieve higher temporal resolution because the interferogram can be recorded rapidly before any experimental scene changes. One of the first static FTS developed in 1965 was based on a modified Michelson interferometer with tilted mirrors [2]. Since then other configurations have been used including cyclic common path (*e.g.*, Sagnac), and Mach-Zehnder interferometers ([3, 4]).

All interferometers rely on the recombination of light that has traversed different optical path lengths. In a traditional Michelson interferometer an OPD between two beams is created by the movement of one mirror relative to another. The beams created by the interferometer are co-linear when they overlap at the detector, creating an interference pattern for each position of the mirror as it is scanned. However, in static interferometry, two beams overlap at an angle at a detector, and the beams traverse different paths through the interferometer. This results in an OPD that changes spatially usually at a focal plane, where a detector array can be placed to record the intensity variation as a function of pixel position within the array. The spectral resolution in both the moving mirror and static optical configuration is nevertheless proportional to the maximum OPD achieved in the system. In the Michelson interferometer this path difference is limited by the maximum distance travelled by one mirror, whereas in a static interferometer the

limit is determined by the length of the array detector and the crossing angle between the two beams. For a detector of given length, the Nyquist frequency determines the largest angle (and therefore highest spectral resolution) that can be achieved. The Nyquist theorem dictates that the highest spatial frequency that can be resolved on the detector requires a minimum of two pixels per interferometer fringe. Therefore, increasing the crossing angle to achieve higher resolution only works up until the Nyquist frequency is reached. In order to overcome the limit of detector resolution, a higher frequency interferogram can be heterodyned to a lower frequency. However, the drawback in using this method is that the increase in the spectral resolution is accompanied by a narrowing of the bandwidth.

Numerous techniques have been developed to implement spatial heterodyne interferometry experimentally. The main approach has been through the use of two reflective blazed gratings in a stationary Michelson setup which has been implemented and described in papers by Dohi and Suzuki [5] and Harlander *et al*. [6]. This technique is typically called Spatial Heterodyne Spectroscopy (SHS). In this technique, the overlap between beams from the same diffraction order ($|m| \geq 1$) creates the interference pattern. SHS has been used in a variety of instruments such as that used in atmospheric remote observation on-board satellites [7], and has been proved to work at a range of wavelengths, from the near UV [7] to long-wave IR [8]. Barnes *et al*. [9] recorded a spatially-heterodyned interferogram by placing a symmetric transmission diffraction grating at an intermediate image plane of two beams created in a Sagnac interferometer. A focussing lens creates an intermediate image plane where the grating is positioned, and a second focussing lens collects beams from certain diffraction orders and images them onto an array detector. Barnes notes that the resolution of the system was dependent on the quality of these two lenses, which introduced optical aberrations and distortions to the system.

In this paper we report on a improved optical design to Barnes' setup [9]. We describe a method to produce a spatially heterodyned interferogram via two different beam configurations by the addition of a single transmission grating. This removes the need for focussing lenses, so that the detector can be placed directly behind the transmission grating, resulting in a more compact instrument. An additional benefit of our technique is that it does not suffer from any extra aberrations introduced into the spectrum by the use of a lens, and different wavelength ranges can be explored by simply changing the grating placed in front of the detector. By using transmission gratings with different groove spacings, spectra of different parts of the electromagnetic spectrum can be recorded, from the UV to the IR.

The present spatial heterodyne technique is complementary to SHS [6] and relies on very similar physics. The use of a single transmission grating for spatial heterodyning (in place of the two reflection gratings used in SHS) at the output port of the interferometer means that the present technique can be used with common-path interferometers (unlike SHS), which have a number of well-known benefits, such as greater stability to vibrations and ease of alignment.

2. Theoretical background and simulations

A beam incident at a transmission grating at an angle, θ_i, creates diffraction orders, m. The specific orders created, and their relative intensities, depend on the grating's groove density, shape, and depth. For a beam at normal incidence on a symmetric transmission grating the positive and negative orders will have equal weights. For the most common groove shapes (*e.g.*, sinusoidal or rectangular), typically the intensities of the diffracted beams created are concentrated in the lower orders ($m = 0$, and $m = \pm 1$). If we consider the grating to be illuminated by two identical coherent beams, arranged so that they have equal but opposite angles of incidence with respect to the transmission grating, the angle can be chosen so that certain diffracted orders are co-linear with each other. Under these conditions, the wavefronts of the diffracted beams will be parallel to each other, so that the resultant overlap between the beams creates no interference fringes (also known as zero spatial frequency). In order for this to occur the rulings of the grating and the

interference fringes need to be parallel.

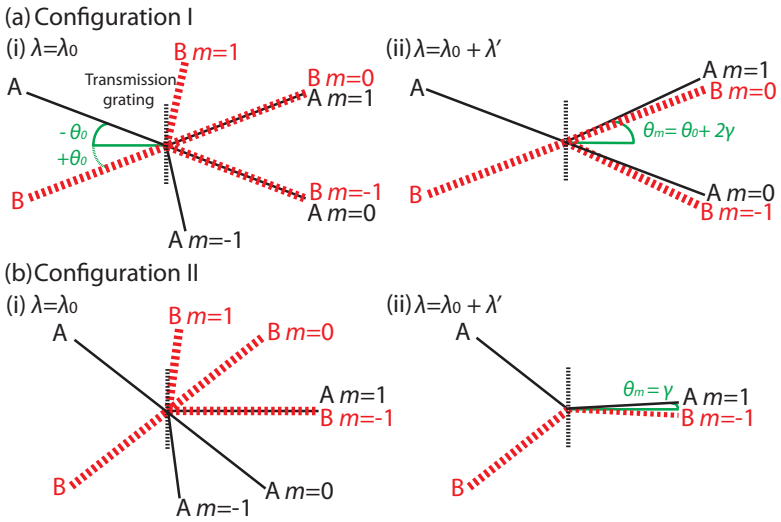

Fig. 1. Illustrations of the configurations required to achieve a heterodyned interferogram from two identical beams (A and B) that are incident at a transmission grating. (a) Depicts Configuration I where the zero and first-order diffracted beams overlap, (i) to give a zero heterodyned frequency when $\theta_0 = \sin^{-1}(\lambda_0/2d)$, whereas in (ii) the diffraction at the grating of both beams at a different wavelength, $\lambda \neq \lambda_0$ will lead to $\theta_m \neq \theta_0$ so that the $m = 0$ beams overlap with two $|m| = 1$ beams at a shallow angle, 2γ, to give a low frequency signal. In Configuration II, (b)(i), the incoming angle is set at $\theta_0 = \sin^{-1}(\lambda_0/d)$ so that only two of the first-order beams will overlap, and are parallel to each other; (ii) depicts the diffraction angles for a different wavelength $\lambda \neq \lambda_0$, so that these first-order beams interact at a shallow angle.

The conditions for the diffracted beams to be co-linear can be derived from the grating equation

$$m\lambda = d(\sin\theta_i - \sin\theta_m), \tag{1}$$

where λ is the wavelength of the light, d the grating spacing, and θ_m the exiting angle of order m. Depending on which orders of the diffracted beams overlap, two different configurations can be achieved.

In the first beam configuration shown in Figure 1(a)(i) we consider two beams of the same wavelength incident at a grating at the same θ_i. As we are using transmission gratings, the sign for m and θ_i will depend on whether the incoming beam is above or below the grating normal. Beam A is above the grating normal so that the incident angle is negative, m is positive on the same side of the grating normal, and negative on the other side. Beam B is below the grating normal so that the signs are opposite. In order to achieve overlap between the zero-order, $m = 0$, of one beam (*e.g.*, beam B) and the diffracted first-order, $m = 1$, of the other (beam A), we set the angle of the diffracted beam to be equal to that of the incident beam. Hence by substituting into Equation 1 we derive the condition

$$\lambda_0 = 2d\sin(-\theta_0), \tag{2}$$

where λ_0 is the wavelength, and θ_0 is the input angle (in this case negative due to beam A being above the grating normal) which are required in order to achieve co-linear beams; this is equivalent to the Littrow condition when using reflective gratings. When both beams of

wavelength λ_0 are incident at the transmission grating at $\pm\theta_0$ there will be two pairs of transmitted co-linear beams from the diffracted and un-diffracted beams.

In Figure 1(a)(ii) the diffraction of both beams (A and B) at a different wavelength, $\lambda = \lambda_0 + \lambda'$, at the grating is considered. The result is the diffraction angle $\theta_m = \theta_0 + 2\gamma$. This small angle difference between the un-diffracted beam, $m = 0$, and the diffracted beam, $|m| = 1$, means that the beam wavefronts will be tilted relative to each other by 2γ. When two wavefronts of wavelength λ cross at an angle 2γ, low frequency (heterodyned) spatial Moiré fringes with a frequency $f = 2\sin\gamma/\lambda$ are produced; it is this heterodyned frequency pattern that we are interested in measuring.

By combining Equation 1 and 2 we get the spatial frequency of the heterodyned Moiré fringes in terms of the angle, θ_0 (derived in the Appendix),

$$f_h = 2\tan\theta_0\left|\frac{1}{\lambda} - \frac{1}{\lambda_0}\right|. \tag{3}$$

Therefore, by increasing θ_0, the heterodyned frequency f_h, and hence the number of fringes across the detector, also increases.

In the second configuration we again consider two beams of the same wavelength, λ_0, incident at a grating at the same θ_i, however in this case, we set the angle such that the two diffracted first-order beams exit the grating along the grating normal, as depicted in Figure 1(b)(i). Here it is the $m = 1$ from beam A (θ_i is negative as it is above the grating normal) and $m = -1$ from beam B (θ_i is positive) that overlap. Therefore, by setting the exiting diffraction angle to zero ($\theta_m = 0$ in Equation 1), the overlap is achieved at an incident angle of θ_0 according to,

$$\lambda_0 = d\sin(-\theta_0). \tag{4}$$

As in Configuration I, if both beams have a wavelength of $\lambda = \lambda_0 + \lambda'$ the beams will be diffracted, in this case at an angle of $\theta_m = \gamma$, as illustrated in Figure 1(b)(ii). As shown in the Appendix, the low frequency Moiré fringes that are formed have a frequency

$$f_h = 2\sin\theta_0\left|\frac{1}{\lambda} - \frac{1}{\lambda_0}\right|. \tag{5}$$

Therefore, in both configurations, higher crossing angles between both beams increase the spectral resolution, whilst the interferogram can be recorded on the array detector. Depending on the specific grating used (and therefore the relative proportion of the beam power that is distributed into each diffracted order, m), some proportion of the input beam is not used, leading to a decrease in the intensity of the interferogram.

2.1. Simulated interferogram patterns

A numerical Fourier propagation model written in MATLAB was used to calculate the transmission from two beams with parallel wavefronts overlapping at a sinusoidal diffraction grating. The results of this model were used to create Figure 2, which shows the exiting of two beams from an aperture width of 1.3 mm and wavelength $\lambda = 3.15$ μm that are incident at a transmission grating with $d = 13$ μm. For both configurations the heterodyne wavelength was set to be $\lambda_0 = 3.00$ μm, and the interaction angle to θ_0. In the first configuration, shown in Figure 2(a), the interaction from the $m = 0$ with the $|m| = 1$ orders from both beams gives a low frequency heterodyned f_h signal. The same conditions for the second setup are shown in Figure 2(b), where the diffracted $m = 1$ from beam A overlaps with the $m = -1$ from beam B.

The simulated interferogram patterns along the detector at two detector positions (marked on Figure 2(a)) in Configuration I are shown in Figure 2(c). If the interaction angles are shallow, then the low frequency signal can be recorded by placing an array detector close to the grating

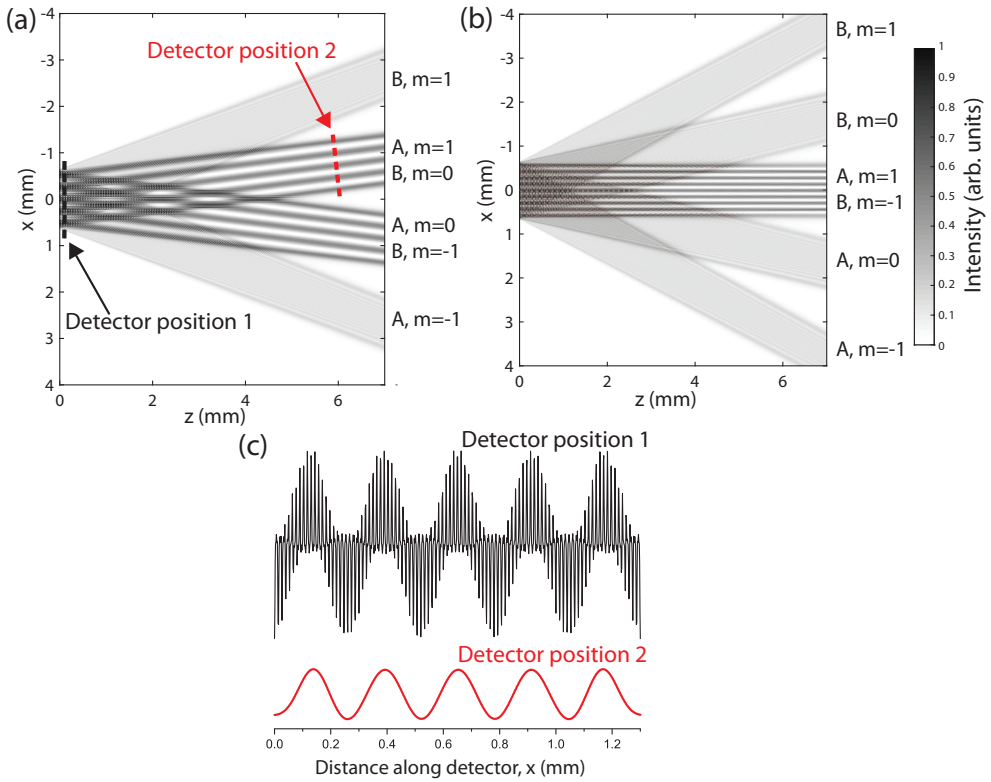

Fig. 2. Simulated setup with both beams at θ_0 and $\lambda = 3.15$ μm, $\lambda_0 = 3.00$ μm, z is the distance from the grating, and x the position along it. The interference pattern created is evident by the low frequency pattern observed when the beams overlap. (a) Depicts Configuration I where the zero and the first-order diffracted beams overlap at a shallow angle. (b) Depicts Configuration II, where only the first-order beams overlap, and the beams are near-parallel to each other. The beams and orders are labelled as in Figure 1. (c) The simulated interferogram pattern across a detector placed at two positions in Configuration I, $z = 0.2$ mm and at an angle at $z = 6$ mm, illustrated in (a).

(position 1). This captures all the frequency components that arise from the overlap of the $m = 0$ and $|m| = 1$ beams, *i.e.*, a total of six beams exiting the grating. However, in most cases, this is not a problem as the lower frequency can be isolated following Fourier transform processing of the interferogram. The grating-detector distance is in the far-field diffraction regime, so no near-field effects are observed (which in this example would occur at approximately $z < 54$ μm). If the angle is larger, the heterodyned frequency can be detected by placing the detector at an angle (position 2 in Figure 2(a)). As this frequency arises due to the overlap of one $m = 0$ and $|m| = 1$ beam the detector is placed where there is minimum overlap with other exiting beams $\sim z = 6$ mm. As the detector remains relatively close to the grating, the grating acts in part as a mask for the incident light, which introduces an additional spatial modulation into the interferogram. This modulation is largely suppressed in the measured interferograms through background-subtraction.

In Configuration II the detector can be placed parallel to the grating at larger z, and the intensity

of the signal will depend on the distribution of light in the diffracted orders. A similar pattern is seen in this case as for Configuration I, in that the interferogram close to the grating will show both heterodyned and non-heterodyned frequencies, whereas beyond the point where there is minimal overlap with the $m = 0$ beams (around $z = 5$ mm), only the heterodyned frequency is detected.

For both configurations, there will be a contribution to the total signal detected from the orders that do not contribute to the heterodyned signal. The increase in the photon-shot noise level brought by this contribution will depend on the overlap of the non-heterodyned beams at the detector, and the percentage of the orders that are transmitted by the grating. To mitigate this issue, it is possible to use custom transmission gratings with a more favourable distribution of the power in the diffracted orders, increasing the ratio of the heterodyned to non-heterodyned signal. For example, in Configuration II a diffraction grating can be used where the power from the zero order is suppressed.

The experimental setup discussed above can be used for a certain range of wavelengths for one grating. However, if a completely different wavelength region is to be studied, a diffraction grating with a different line spacing must be used, and, depending on the frequency required at the detector, the angle between the two beams must be changed as well.

In the experiments described in this paper, Configuration I was used with very shallow crossing angles, and the detector placed parallel to the grating in position 1 (Figure 2(a)). The incoming angle was chosen for a specific λ by taking into account the frequency, f_h, required at the detector to satisfy the Nyquist sampling criterion.

2.2. Throughput simulations

In order to assess the throughput performance of the proposed system, ray tracing (Zemax) models of two interferometers were set up, a modified Sagnac interferometer (described in Section 3), and a Spatial Heterodyne Spectrometer (SHS) [6]. Both interferometers provide heterodyned interferograms, the SHS by the use of diffraction gratings instead of mirrors, whereas the Sagnac was heterodyned by placing a transmission grating in front of the array detector (as described in Section 2). The input optics, detector, and grating groove density for the two setups were set to be identical, however appropriate imaging lenses were added to the SHS system. In order to achieve the same spectral range of operation the same heterodyning wavelength was set for both systems. By changing the angle of the source rays within the dispersion plane with respect to the optical axis (the off-axis angle, β), two parameters were studied.

Firstly, the change in the optical wavelength was calculated with respect to the β. The change in the output wavelength compared to the input for an $\beta = 1.1^\circ$ was 0.2% for the heterodyned Sagnac. However, no noticeable change in the wavelength for the SHS system was calculated.

Secondly, the maximum β where the interferogram fringes contribute constructively to the interferogram was calculated. The SHS model returned an acceptance of off-axis angles which was an order of magnitude greater than that of the heterodyned Sagnac in Configuration II, and five times that of Configuration I. Configuration II may have worse throughput because the incidence angle is around double that of Configuration I for the same conditions ($c.f.$ Equations 2 and 4).

Therefore it would be expected that experimentally, for the same conditions, the SHS would show a higher throughput and spectral resolution compared to the heterodyned Sagnac interferometer.

3. Experimental results

The theoretical concept from Section 2 was experimentally verified by assembling a static interferometer, as illustrated in Figure 3(a). This Sagnac-type interferometer [10] was chosen as it is lens-free, and the angle between the beams can be controlled at the detector. Incoming light from a multimode fibre optic bundle (Thorlabs BF20HSMA01) is expanded (Thorlabs

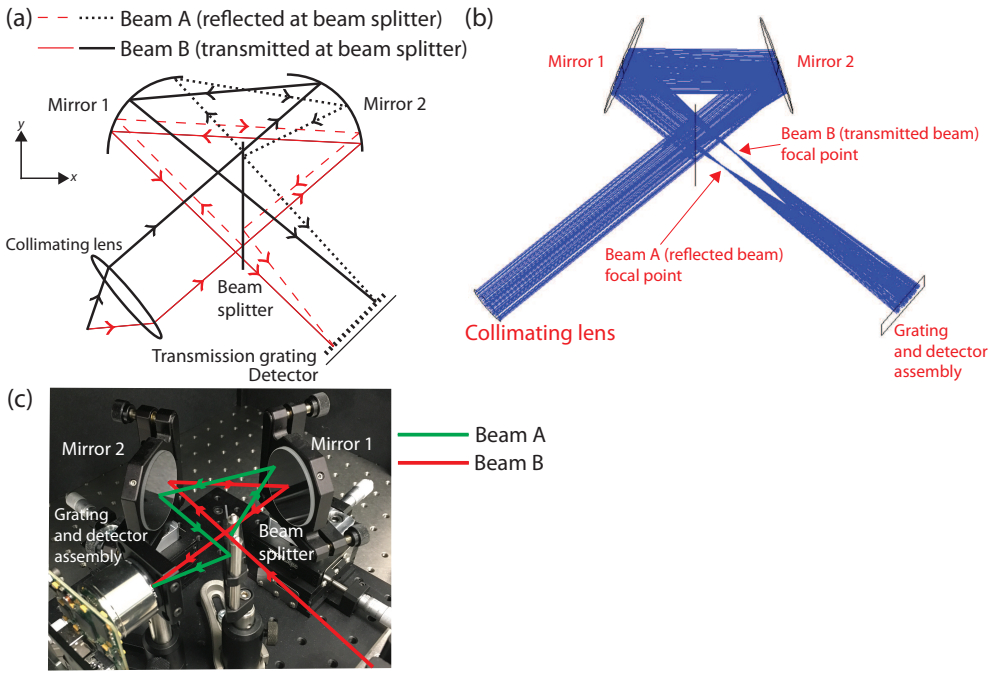

Fig. 3. (a) The experimental setup, (b) the corresponding ray tracing model, and (c) picture of experimental apparatus and example rays for both beams.

BE02-05-A) into free space before being split by a beam splitter (Thorlabs BSW27). One beam (beam A) is reflected by the beam splitter and travels clockwise onto two concave cylindrical mirrors (Thorlabs CCM254-200-P01), before being reflected again by the beam splitter towards the detector. The second beam (beam B) travels anti-clockwise and is transmitted by the beam splitter towards the detector. At the image plane a symmetric transmission grating (Edmund Optics transmission grating beam splitter, 46-069, 80 grooves mm^{-1}) was placed. The detector, a CMOS camera (Mightex SME-B050-U), was placed directly behind the transmission grating, at a distance of $\sim$ 1 mm. The detector has an array of 2560 $\times$ 1920 pixels (horizontal $\times$ vertical), with a pixel width of 2.2 μm. The interaction angle between both beams was changed by moving Mirror 1 along the x direction, and rotating Mirror 2 in the xy plane to ensure that the beams overlap uniformly at the grating. Both beams A and B have focal points next to the beam splitter, as shown using a ray tracing (Zemax) model of the setup in Figure 3(b). As the mirrors are moved, the distance between these two focal points increases, and can be measured experimentally. By knowing this distance and the distance from this point to the image plane, the experimental interaction angle can be calculated. This angle can then be verified by comparing the experimental and simulated interferograms. The experimental interferograms are produced by full vertical binning, with an integration time of four seconds. Two background signals, one each from the reflected and transmitted beam (Beam A and B) are obtained by experimentally blocking the beams alternately at their focal points (noted on Figure 3(b)). The final background-subtracted interferogram is created by subtraction of both of these signals from the interferogram obtained with both beams overlapping at the detector.

An example of the signal acquired on the array detector is shown in Figure 4. A bandpass transmission filter centred at 580 nm (Thorlabs FB580-10) is placed after both a tungsten halogen lamp (Ocean Optics LS-1), and a mercury argon lamp (Ocean Optics HG-1), with both beams overlapping at the grating at a relatively low interaction angle of $\theta_i = 1.4°$. The corresponding

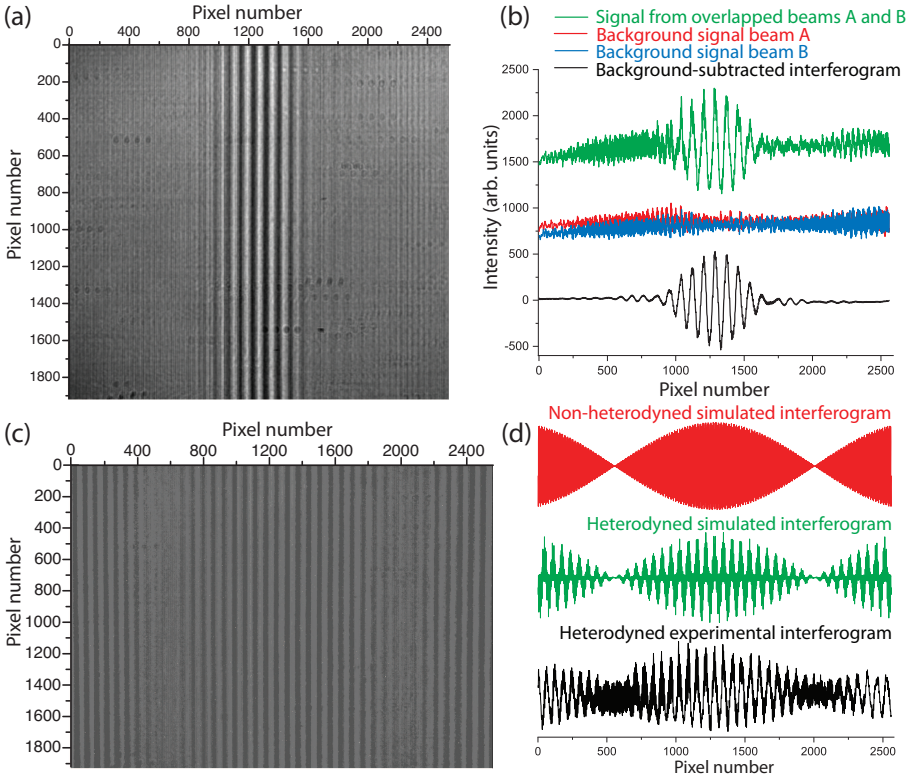

Fig. 4. (a) The experimental signal at the array detector from a tungsten halogen lamp, and (b) the corresponding vertically-binned signal from the overlapping beams, the background signals from beam A and B, and background-subtracted interferogram. Figure (c) is the experimental signal for a mercury argon lamp, and (d) the corresponding background-subtracted interferogram and the simulated results. All spectra were taken with a 580 nm filter in the beam path.

background-subtracted interferograms are also shown. The spectrum of the tungsten halogen lamp is dominated by the filter which has a large full width at half maximum (FWHM) of 10 nm, resulting in the detected interferogram having a fixed width. However, the mercury argon lamp emits a doublet centred at $\lambda = 578$ nm which has a sharp spectral profile so there is little decay in the interferogram over the detector length. The simulated interferograms at $\theta_i = 1.4°$ with and without the grating for this source are also shown in Figure 4(d), where the input spectral line positions were taken from Ref. [11], the beam diameter matched the detector, and the FWHM of the spectral line was set to be narrower than the resolution expected by the interferometer. By comparing the heterodyned experimental and simulated interferograms, both the lower (heterodyned) and higher (non-heterodyned) frequency patterns are seen to match well, and the positions of the nodes arising from the doublet are reproduced well. Note that both the higher and lower frequencies are present in the heterodyned interferograms, similar to that seen in the simulations in Figure 2(c). The high frequency component visible around pixel numbers 500 and 2000 in the experimental interferogram corresponds to the grating frequency (which is not quite totally suppressed by the background-subtraction described above). The interferograms have been offset for clarity, and the experimental results have been scaled to give similar visibility to the simulated results.

Ray tracing (Zemax) shows that that some deviation from planarity of the wavefronts is

introduced by the symmetry-breaking translation of one of the mirrors relative to the other during alignment of the interferometer (which is performed to separate the focal points of the interfering beams, see Figure 3(b). However, this deviation is small ($e.g.$, $< 1\%$ at 580 nm and $\theta_i = 1.4°$) and varies linearly across the 5 mm detector array, which means that the deviation can be compensated for by rotating the detector by a small amount. Astigmatism arising directly from the curvature of the mirrors is minimal for the weak focussing powers used in our experiments. However, in practise, small misalignments of the interferometer may further artificially broaden the experimental spectral features by a small amount and this remains a topic for future study.

Throughout the paper, no apodization has been applied to the interferograms in order to show the true width of the corresponding spectral profiles. In addition, detector calibration has not been performed to take into account effects such as shot noise, thermal effects, and pixel sensitivity variation, which would affect the relative intensities of the interferograms.

3.1. Spatially-heterodyned experimental signal

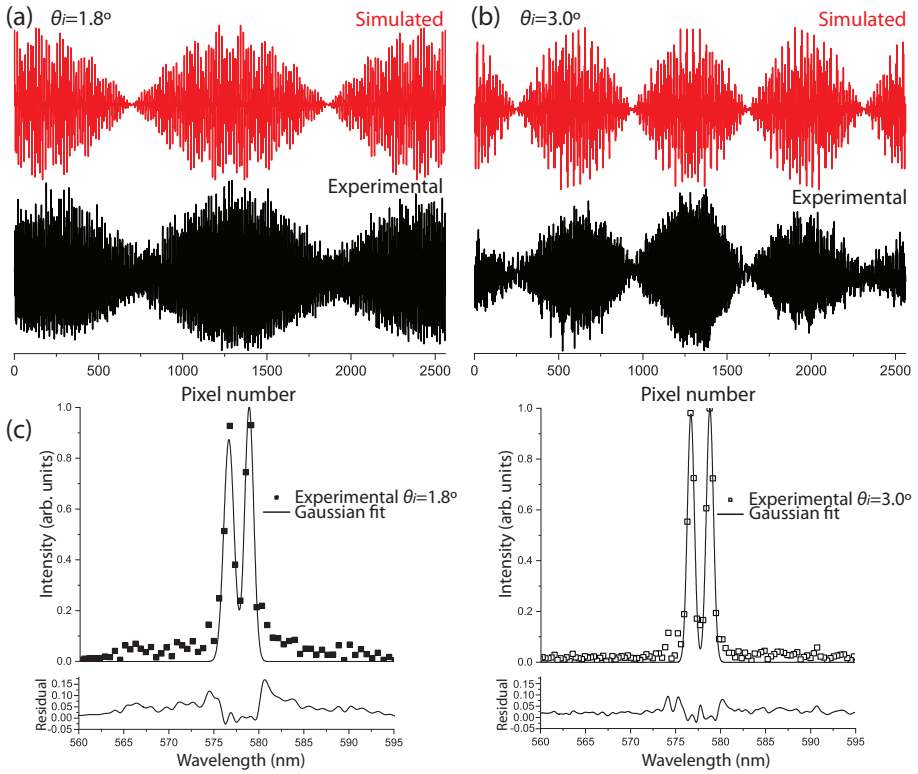

Fig. 5. The normalised experimental and simulated interferograms for the yellow mercury doublet centred at $\lambda = 578$ nm where the beams from the interferometer setup are incident at the transmission grating at angles of (a) $\theta_i = 1.8°$, and (b) $\theta_i = 3.0°$. (c) The corresponding normalised experimental spectra.

In order to approximate the response of the instrument to a single frequency, the emission from the yellow mercury doublet was measured by using the mercury argon lamp and a 580 nm bandpass filter. At this wavelength the detector-limited maximum interaction angle is $\theta_i = 1.9°$, however the grating decreases the measured frequency so that the interaction angle can be increased to $\theta_i = 3.2°$. The experimental and simulated interferograms for angles of $\theta_i = 1.8°$ and $\theta_i = 3.0°$ are shown in Figure 5. The simulated interferogram has been produced by

taking into account only the frequencies from the doublet. The overall shape and frequency of the simulated interferograms matches the experimental interferograms well. The higher (non-heterodyned) frequency is not present in these interferograms as the frequency produced at these larger angles is too high to be observed on this detector.

Figure 5(c) shows the corresponding experimental Fourier transformed spectra together with a double Gaussian fit and the residuals from the fit. In order to assess the experimental FWHM values, the same double Gaussian fit was performed on spectra retrieved from simulated interferograms by the theoretical method described in Section 2. The Gaussian-fitted FWHM of the spectral line at $\lambda = 576.96$ nm for the experimental (simulated) result at $\theta_i = 1.8°$ is 1.35 nm (1.09 nm), and at $\theta_i = 3.0°$ is 0.92 nm (0.74 nm). This is an experimental (simulated) resolving power of 627 (780). Therefore, the width of the spectral lines decrease as the angle increases, although the experimental values are too large compared to the simulated widths by around 20%, the difference most likely arising from the uncertainty in the crossing angle of the two beams.

4. Discussion and conclusion

This paper describes a method to modify static interferometer designs to achieve a higher spectral resolution. This is done by the addition of one optic, a symmetric transmission grating, close to the array detector which has the effect of heterodyning the interferogram to lower frequencies. Experimental results from the mercury spectral line at $\lambda = 576.96$ nm show a decrease in the FWHM of the detected line from 1.35 nm to 0.92 nm for a change in the interaction angle from $\theta_i = 1.8°$ to $\theta_i = 3.0°$. The experimental results were achieved with a 80 grooves mm^{-1} transmission grating and a 2560 pixel camera. All equipment was bought "off-the-shelf" for this proof of concept demonstration.

The setup can be modified for the experimental requirements. For example, if two wavelengths that differ by 2λ are to be explored simultaneously, this can be achieved at one θ_i by the placement of a detector at an angle (using Configuration I) and parallel (Configuration II) to the grating, at detector positions similar to that depicted in Figure 2(a). If the wavelengths are closer together, multiple gratings with different groove spacings could be interchanged to focus on each wavelength region separately, whilst maintaining the same θ_i. This could also be achieved with one custom grating which has regions with different groove spacings stacked vertically to make use of the two dimensional detector. The technique can be used in different wavelength regions (*e.g.*, UV, visible and IR), by using suitable optical components and detectors. An additional feature is the possibility to increase the bandwidth (with the corresponding decrease of the spectral resolution) by rotating the grating about the grating normal, so that the rulings are no longer parallel to the interferogram fringes.

The spatial heterodyning method described in this paper is perhaps most useful for instruments that operate in the mid to far-IR, and this is the ultimate goal of this research. For example, at an interaction angle of $\theta_i = 3°$ the spectral resolution for light at a wavelength of $\lambda = 3$ μm can be enhanced by a factor of 20 with a $d = 30$ μm grating. The instrument described in this paper is also suited to applications in which weight and cost are important as the number of focussing optics is kept to a minimum. One additional motivation for the spatial heterodyne technique is that it can be applied (e.g., retrofitted) to existing designs of static interferometer straightforwardly, thereby allowing these designs to be "fine-tuned" for certain applications. The interferometer design can be *e.g.*, reflective common-path (demonstrated here) and non-common-path [12] instruments, or Wollaston-based polarisation division interferometers (similar to Ref. [13]).

Appendix

To derive the frequency of the heterodyned fringes for a specific λ in terms of our input angle, θ_0, for Configuration I, Equation 1 and 2 are combined. From Figure 1, we consider the frequency

from $m = 0$ of beam B overlapping with $m = 1$ of beam A, and $\lambda > \lambda_0$,

$$\frac{\lambda}{d} = \sin(-\theta_0) - \sin(\theta_0 + 2\gamma),$$

assuming that γ is small so that $\cos 2\gamma \approx 1$, and by substituting $\sin\theta_0$ with Equation 2,

$$2\sin\gamma = \frac{\lambda_0 - \lambda}{d\cos\theta_0}.$$

Now, $f = (2\sin\gamma)/\lambda$, so that

$$f = 2\tan\theta_0\Big(\frac{1}{\lambda_0} - \frac{1}{\lambda}\Big).$$

If $\lambda < \lambda_0$ then the diffracted angle is $\theta_m = \theta_0 - 2\gamma$ for the same conditions, and we get

$$f = 2\tan\theta_0\Big(\frac{1}{\lambda} - \frac{1}{\lambda_0}\Big),$$

so that, in general,

$$f_h = 2\tan\theta_0\Big|\frac{1}{\lambda} - \frac{1}{\lambda_0}\Big|.$$

This result is half the frequency that is typically obtained in SHS [6]. For Configuration II the corresponding frequency created from the $m = 1$ of beam A overlapping with the $m = -1$ of beam B is

$$f_h = 2\sin\theta_0\Big|\frac{1}{\lambda} - \frac{1}{\lambda_0}\Big|.$$

Funding

Royal Society (Dorothy Hodgkin Fellowship DH130096); Science and Technology Facilities Council (STFC) Proof of Concept Fund (POCF1617-04).

Disclosures

The authors declare no conflicts of interest.

References

1. P. R. Griffiths and J. A. De Haseth, "Fourier transform infrared spectrometry", John Wiley & Sons (2007).
2. G. W. Stroke and A. T. Funkhouser, "Fourier-transform spectroscopy using holographic imaging without computing and with stationary interferometers", *Phys. Lett.* **16**(3) 272–274 (1965).
3. W. H. Steel, "Interferometry", Cambridge University Press (1983).
4. M.-L. Junttila, J. Kauppinen, and E. Ikonen, "Performance limits of stationary Fourier spectrometers", *J. Opt. Soc. Am. A* **8**(9) 1457–1462 (1991).
5. T. Dohi and T. Suzuki, "Attainment of high resolution holographic fourier transform spectroscopy", *Appl. Opt.* **10**(5) 1137–1140 (1971).
6. J. Harlander, R. J. Reynolds, and F. L. Roesler, "Spatial heterodyne spectroscopy for the exploration of diffuse interstellar emission lines at far-ultraviolet wavelengths", *Astrophys. J.* **396**(2) 730–740 (1992).
7. C. R. Englert, J. M. Harlander, C. M. Brown, and K. D. Marr "Spatial heterodyne spectroscopy at the Naval Research Laboratory", *Appl. Opt.* **54**(31) F158–F163 (2015).
8. C. R. Englert, D. D. Babcock, and J. M. Harlander "Spatial heterodyne spectroscopy for long-wave infrared: first measurements of broadband spectra", *Opt. Eng.* **48**(10) 105602 (2009).

9. T. H. Barnes, T. Eiju and K. Matsuda, “Heterodyned photodiode array Fourier transform spectrometer”, *Appl. Opt.* **25**(12) 1864–1866 (1986).
10. A. Hugh Mortimer “Compact interferometer spectrometer”, U.S. Patent 9046412 B2 (June 2, 2015).
11. A. Kramida, Y. Ralchenko, J. Reader, and NIST ASD Team. NIST Atomic Spectra Database (ver. 5.3), [Online] (2015).
12. M. Schardt, P. Murr, M. Rauscher, A. Tremmel, B. Wiesent, and A. Koch, “Static Fourier transform infrared spectrometer”, Opt. Express **24**(7), 7767–7776 (2016).
13. M. W. Kudenov, M. N. Miskiewicz, M. J. Escuti, and E. L. Dereniak, “Spatial heterodyne interferometry with polarization gratings”, *Opt. Lett.* **37**(21), 4413–4415 (2012).